

Robust Control of a MEMS Probing Device

Xuemeng Zhang, Bonjin Koo, Srinivasa M. Salapaka, Jingyan Dong, and Placid M. Ferreira

Abstract—In this paper, a systematic design based on the robust control theory is developed for a microelectromechanical systems nanopositioning/probing device. The device is fabricated on a silicon-on-insulator substrate, and provides decoupled XY motion by using a parallel kinematics mechanism design. Each axis of the device is actuated by linear comb-drives and the corresponding displacements are sensed by separate comb structures. To improve the sensing resolution, the sensing and driving combs are electrically isolated. The nonlinear dynamic model between the actuation voltage and the sensed displacement will increase the complexity of model identification and control design. We circumvent the nonlinear model by redefining the input and output (I/O) signals during the model definition and identification, which results in linear and time-invariant models. A dynamical model of the system is identified through experimental input–output frequency-domain identification. The implemented H_∞ control design achieves a significant improvement over the response speed, where the bandwidths from the closed-loop sensitivity and complementary sensitivity functions, respectively, are 68 and 74 Hz. When compared to open-loop characteristics, enhancement in reliability and repeatability (robustness to uncertainties) as well as noise attenuation (by over 12%) is demonstrated through this design.

Index Terms—Electrostatic comb drive, H_∞ control, microelectromechanical systems (MEMSs), nanopositioning, system identification.

I. INTRODUCTION

IN microelectromechanical system (MEMS) devices, capacitive structures which consist of electrostatic combs are being widely used as actuators and sensors in positioning and probing devices, since first introduced by Tang *et al.* [1]. Comb drive actuators, when compared to piezoelectric and shape-memory-alloy actuators, provide several advantages that include ease of fabrication and integration into MEMS devices. Moreover, electrostatic comb drives have faster response and are easy to

operate and control because the driving forces do not depend on actuator position but only on the applied voltage.

For fast nanoscale scanning applications, a high-resolution sensing scheme to accurately sense the manipulator displacement is a critical requirement. The displacement or corresponding capacitance change in comb structures is usually very small (less than 1 pF), which makes the sensing system design difficult. An optical sensor based on laser diode implemented by Borovic *et al.* [2] decouples the sensing from actuation; however, it gives limited linear operating range. A simultaneous actuation and sensing scheme was successfully implemented by Dong and Ferreira [3], where however the sensing speed is limited by the sensing circuit. Other sensing schemes such as microscopes [4] and atomic force microscopes (AFMs) have also been used to detect the displacement of comb drives, but predominantly for device characterization. None of them have been used within a high-bandwidth feedback control scheme. The success of model-based feedback control designs [5]–[11] in scanning probe microscopy provides motivation for employing advanced control designs to MEMS-based devices. Furthermore, advanced control designs are necessary to exploit high-resolution capabilities achieved by recent advances in on-chip capacitance sensing [12], [13] and translate them to high-resolution high-bandwidth reliable positioning of MEMS devices using comb structures.

The main performance objectives of the control design for nanopositioners are to achieve high positioning resolution, high bandwidth, and good robustness to model uncertainties. Most commercially available nanopositioning devices do not have high bandwidth for high rate operations. For example, nano scanners used in the AFMs generally only have a closed-loop bandwidth less than 10 Hz. The need for simultaneously achieving these multiple objectives under hardware constraints (such as control signal saturation) and fundamental design limitations (e.g., Bode integral law) necessitates careful feedback control design. The robust-control framework allows for translating the aforementioned performance objectives into an optimization problem that can be solved to obtain a controller meeting the specifications (that is, when such a controller exists). In this paper, we present a control design under this framework, where the implemented controller and the resulting closed-loop device achieve significant improvements in bandwidth, noise attenuation, and robustness.

This paper is organized as follows: In Section II, a description of the MEMS probing device, the hardware setup, and a derivation of the mathematical models for the electrostatic comb drives and displacement sensors are presented. In Section III, the model of the device is identified parametrically, based on frequency-domain identification method, and then simplified by a model reduction method. In Section IV, H_∞ -control design methodology is briefly described and a controller is developed.

Manuscript received March 26, 2012; revised September 7, 2012; accepted October 7, 2012. Recommended by Technical Editor S. Fatikow. This work was supported by the National Science Foundation (NSF) under Grant CMMI 0800863 and Grant ECCS 0925701, and by the NSF-sponsored Center for Nanoscale Chemical-Electrical-Mechanical Manufacturing Systems under Award CMMI-0749028.

X. Zhang was with the Department of Mechanical Science and Engineering, University of Illinois at Urbana-Champaign, Urbana-Champaign, IL 61802 USA. He is now with Elettric 80, Inc., Skokie, IL 60076 USA (e-mail: xuemengzhang1986@gmail.com).

B. Koo, S. M. Salapaka, and P. M. Ferreira are with the Department of Mechanical Science and Engineering, University of Illinois at Urbana-Champaign, Urbana-Champaign, IL 61802 USA (e-mail: bonjin.koo@gmail.com; salapaka@illinois.edu; pferreir@illinois.edu).

J. Dong is with the Department of Industrial and Systems Engineering, North Carolina State University, Raleigh, NC 27695-7906 USA (e-mail: jdong@ncsu.edu).

Color versions of one or more of the figures in this paper are available online at <http://ieeexplore.ieee.org>.

Digital Object Identifier 10.1109/TMECH.2012.2224122

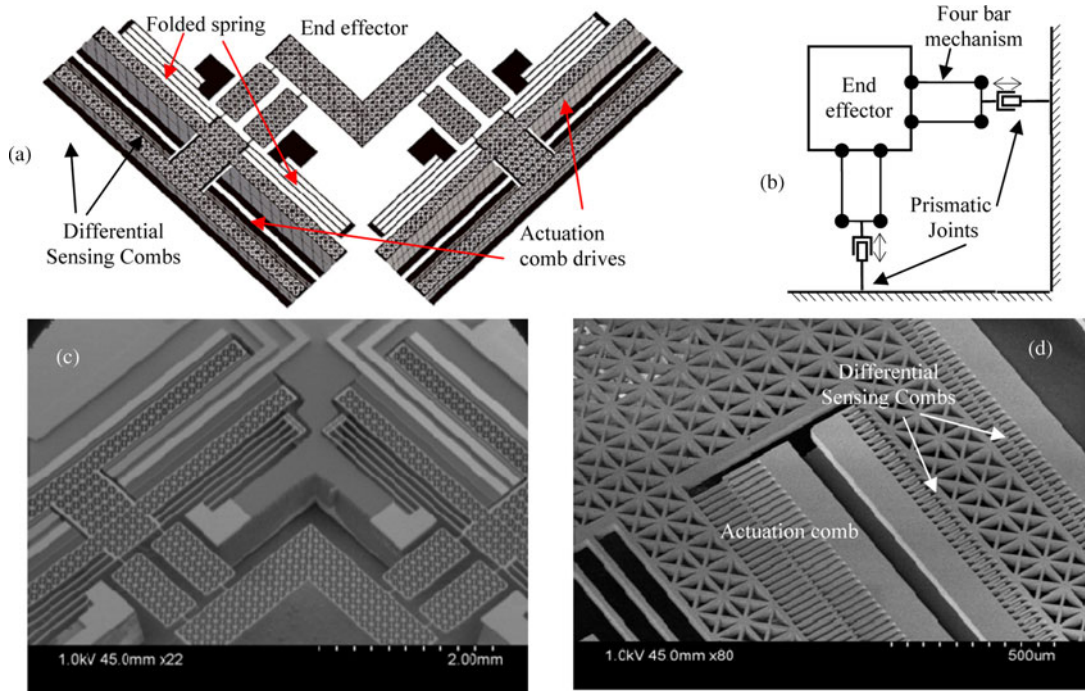


Fig. 1. (a) Schematic diagram of XY micropositioning stage. b) Kinematic model the stage. c) SEM pictures of the stage. (d) Actuation/sensing combs.

Section V presents the controller implementation, experimental results, and the corresponding analysis. In Section VI, conclusions are drawn from results obtained in this paper. Future directions are also discussed.

II. DEVICE DESCRIPTION AND MATHEMATICAL MODEL

The lateral (XY) positioning MEMS device with the comb-drive actuator and capacitive sensor is shown in Fig. 1. The kinematic design of the MEMS device is based on a parallel kinematic mechanism (PKM). Our device design has two independent kinematic chains that connect the end-effector to the base. Each kinematic chain includes two serial-connected components: a prismatic joint that provides pure translational motion and a parallelogram four-bar linkage mechanism that provides rotary displacement while holding the orientation of the end-effector invariant. These two chains are placed perpendicular to each other, so as to kinematically decouple the two actuated joints to the maximum extent possible. The PKM design [see Fig. 1(b)] decouples the motion in the X- and Y-axis and restricts rotations in the XY plane while allowing for a large motion range with linear kinematics [14]–[17]. The end-effector of XY stage, shown in Fig. 1(a), can move independently along two perpendicular axes. Linear comb drives with folded springs in each axis provide the required linear actuation. Parallelogram four-bar linkages absorb coupled motion of the two axes while simultaneously confining the orientation of the end-effector. The results reported from our previous work [14]–[17] demonstrated the decoupled motion of XY directions. As a result, control design can be simplified, and controller can be designed for each axis individually. The electrostatic forces produced by the

actuation comb drives overcome the resistance of flexure hinges and folded springs to produce the desired motion with a specific actuation voltage. The overall device is fabricated on a silicon-on-insulator die with a 50- μm thick device layer and a 3- μm thick buried oxide layer. The high aspect-ratio structures, such as comb fingers and folded springs, are fabricated by deep reactive ion etching (DRIE).

In our specific device design, the linear comb drives have 188 finger pairs, with the height of each finger of 50 μm , and the gap between interdigitated fingers of 5 μm . The comb drive actuators provide an electrostatic force of 81.5 μN at 70 V, and, produce a displacement of 22 μm of the stage. The stage has built-in differential capacitance sensing combs for each axis. Besides the actuation comb drives, two pair of sensing combs are fabricated to facilitate a differential sensing scheme (see Fig. 1) and thus enhance signal-to-noise ratio (SNR) for better resolution. For our system, most of noises come from the sensing circuits with constant amplitude. By using differential sensing scheme with two pair of sensing combs, the output of displacement sensing is doubled, compared with just using one pair of sensing combs. Thus, the SNR is improved by a factor of 2.

In this paper, the actuation comb drive and sensing comb structures are designed in tandem with control system. In the most devices in the existing literature, the actuating and the sensing combs are electrically connected together. This imposes an impediment in circuit design since the actuator requires high actuation voltage (typically more than 50 V) while the sensing signal usually is less than 5 V. To reduce the interference between actuation and sensing circuits, the sensing and the actuation combs are mechanically separated and electrically disconnected in the device layer, but are mechanically connected

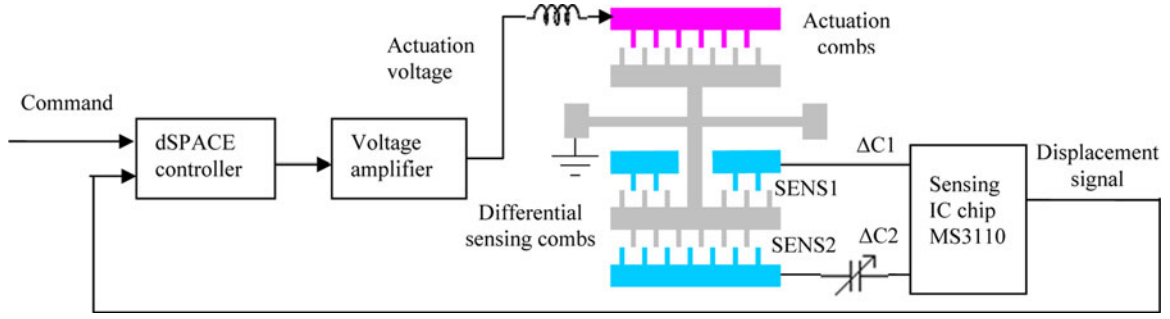


Fig. 2. Circuit diagram for the actuation and sensing needed for control implementation.

together by an underlining connection pad that is composed of the insulation SiO₂ layer and partially etched handle layer silicon. The capacitance change resulting from the differential sensing combs, which is proportional to the displacement of the axis, is measured by a capacitance-to-voltage chip, the MS3110 universal capacitive readout IC (resolution of 4 aF/ $\sqrt{\text{Hz}}$ and range up to 10 pF).

The differential capacitance sensing-comb system is specifically designed with two opposed combs so that motion of the axis reduces the finger overlap (and hence, capacitance) for one comb while increasing that for the other. Two sensing combs, SENS1 (188 fingers) and SENS2 (156 fingers), have the same finger height (50 μm) and the gap between adjacent fingers (5 μm). However, the initial overlap between the moving and stationary fingers for SENS1 and SENS2 is different and they are 30 and 10 μm , respectively. With a displacement of 10 μm , corresponding change in capacitance for SENS1 and SENS2 is 0.167 and 0.138 pF, respectively. Therefore, the differential change in capacitance is 0.305 pF and theoretically the sensing comb will produce a capacitive change rate, $\Delta C/\Delta X$, of 0.0305 pF/ μm with air being the medium between the comb fingers. In our device, a displacement of 20 μm is produced by the actuation voltage of 100 V for actuation comb drive and $\Delta C/\Delta X$ of 0.0136 pF/ μm is experimentally measured for differential sensing comb drives because of increased gap between interdigitated fingers due to overetching in the DRIE process (see [16] for more details).

The capacitance difference SENS1–SENS2 is detected by the on-chip sensor MS3110 as an analog voltage. The feedback signal from MS3110 is further read into dSPACE (DS1104) controller with 16-bit A/D and D/A conversion modules. Also, dSPACE offers real-time interface and drivers that allow user to design control systems in Simulink and then compiles it into C code that is downloaded into and run by the dSPACE embed controller (DS1104). The control commands are given by DS1104 and further amplified by a power amplifier to drive the actuation comb drive, which completes the feedback loop.

The circuit diagram of system setup is shown in Fig. 2. The two sensing comb in our MEMS device, SENS1 and SENS2, are connected to the differential inputs, CS1 and CS2, respectively, with the common ground connected to COM port on the sensor. A tunable capacitance is included in parallel with the

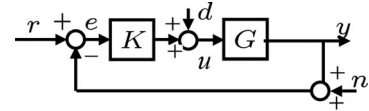


Fig. 3. Control block diagram of the closed-loop device.

decremental sensing comb, SENS1, in order to offset the capacitance difference between two inputs so that it lies within the range of sensor measurement (less than 10 pF). The sensor output is read by one of the A/D channels of the dSPACE control board which processes the designed control algorithm. The generated control command is amplified by 20 times which is transduced into the electrostatic force by the comb that drives the MEMS stage. A 5-V battery is used for powering MS3110 sensor to avoid line noise in the sensing circuit.

Fig. 3 shows a block diagram of the closed-loop system. Here, the reference or the command signal is represented by r ; the input signal to the actuation system and plant is denoted by u , the sensor reading by $y + n$, where n is the sensor noise, d denotes the mechanical disturbances, e denotes the error signal—the difference between the reference and the output signals; and the transfer function G represents the MEMS device comprising of the actuation, stage, and detection stages, and the transfer function K represents the controller transfer function.

A. Mathematical Model

The force that drives combs and the MEMS stage is given by

$$F = n \frac{\epsilon t}{g} V^2 \quad (1)$$

where n is the number of fingers in the comb drive, ϵ is the permittivity of free space, t is the thickness of fingers, g is the gap between fingers, and V is supply voltage. The dynamics of the electrostatic drive and the actuated mechanical structures is governed by a second-order mass-spring-damping system [3]

$$f = m\ddot{\delta} + b\dot{\delta} + k\delta \quad (2)$$

where f is the input force, m is the mass, b is the damping coefficient, k is the spring constant, and δ is the length that comb has traveled. By applying Laplace transform, the dynamic

equation in (2) becomes

$$\frac{\Delta}{F} = \frac{K\omega_n^2}{s^2 + 2\xi\omega_n s + \omega_n^2} \quad (3)$$

where K is the dc gain, ξ is the damping ratio, ω_n is the natural frequency of the MEMS stage. Further, the linear translation of comb drive results in a linear change of the capacitance for the sensing comb given by

$$\Delta C = n \frac{\varepsilon t}{g} \delta. \quad (4)$$

The sensor output is linear with the capacitance change [18]. The output voltage of sensor with respect to capacitance change is given by

$$V = \gamma \frac{CS_2 - CS_1}{C_f} + V_{\text{off}} \quad (5)$$

where V is the sensor output, C_f is the feedback capacitance inside sensor which is tunable, γ is the tunable gain, V_{off} is tunable offset voltage.

Therefore, in this setup, the driving force generated by the driving comb is proportional to V^2 . The mechanical response of XY stage is essentially that of an underdamped second-order system. The linear translation of the comb results in a linear change in capacitance, which is further converted to a linear change in voltage by the MS3110 IC.

III. MODEL IDENTIFICATION

A. Sine Sweep Method and Experiment Results

From the discussion in Section II, the driving force generated by the comb drives is proportional to V^2 . If actuation voltage is directly used as the input signal to the plant, the resulting nonlinear dynamic model will bring many difficulties in controller design. We design a new variable $u = V^2$ as the input of the plant to avoid this problem. The dynamic system that maps the plant input $u = V^2$ to the output δ , the displacement of electrostatic comb, can be modeled by a second-order linear underdamped differential equation; except for certain nonlinearities such as fringe effects from the finite dimensions of the capacitors. In the robust control approach used in this paper, these nonlinearities, measurement noise, disturbance, parametric uncertainties, and other modeling uncertainties are considered as perturbations about the previous linear model. In this approach, the control is designed to make the closed-loop system insensitive to these uncertainties in addition to obtaining the performance objectives on the bandwidth and the positioning resolution.

To obtain a dynamic system model of the positioning stage, we used the sine-sweep frequency-domain identification method. The main idea is to excite the system with sinusoidal inputs over a range of frequencies, obtain the corresponding system responses, and then fit a corresponding dynamic systems model (an ordinary differential equation) that has the same input-output behavior. We implemented this method using a dynamical system analyzer (DSA) which provides sinusoidal inputs from one channel and collects the responses at the other (see Fig. 4).

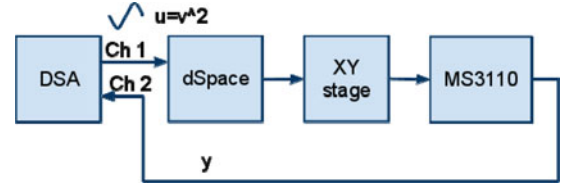


Fig. 4. Experiment setup for system identification.

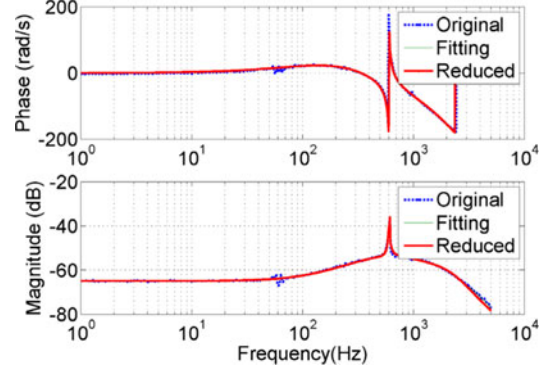


Fig. 5. Model identification results compare frequency response data, identified model and reduced model.

The DSA sends out sinusoidal signals with frequencies ranging from low to high. The nonlinearity between the excitation voltage and the plant output (displacement) makes the mode identification using a DSA nontrivial problem. Especially, steps have to be taken to correctly identify a linear dynamic model between V^2 and displacement where V is the supply voltage to comb drive. In order to account for this nonlinearity, we did not directly feed the signal from DSA channel directly to comb drive but modified it in dSpace, so as to capture the linear behavior between the actuation force and the resulting displacement. Within dSpace, we first took the square root of the signal from Channel 1 (say v_1) and then multiplied $\sqrt{v_1}$ by 1/200 to neutralize the scaling factors from the D/A conversion (by 10) and power amplification (by 20). Note that there is also a scaling factor of 1/10 during the A/D conversion. Therefore, in dSpace programming, the input from the A/D conversion is multiplied by 10 to recover the signal v_1 from Channel 1. The supply voltage sent out to the comb drive is thus $\sqrt{v_1}$. As shown earlier, the system has a linear model with input V^2 , and therefore with the signal v_1 . Sensor reading is recorded by Channel 2 of the DSA. The DSA then estimates the system response (magnitude and phase shift) at each chosen frequency. The data rate of the dSpace system can be as high as 50 kHz. Therefore, the sweeping range was set to be 1 Hz to 25 kHz to prevent aliasing. The frequency resolution is set to be 100 points per decade. The resulting system is shown in Fig. 5.

Based on the mathematical model previously derived, the system ideally is an underdamped second-order system with expected low damping ratio. Based on the experiment results shown in Fig. 5, a peak in magnitude appears at a frequency of around 600 Hz and the magnitude (around 10 dB) of the peak indicates a small damping ratio. However, MEMS probing/positioning devices are usually complex systems with which

mathematical models do not match completely. For example, the fringe effect which characterized the nonlinearity of the magnetic field existing between charged comb fingers is usually ignored during linear system modeling. Hinges and folded springs may also embed complex dynamics. The experimental results also indicate a much higher order dynamics inside the system. Model fitting algorithms are thus brought in to obtain a parametric model of the device.

B. Model Fitting

From the bode plot obtained from the previous identification scheme, it can be deduced that the number of poles exceeds that of zeros only by 2 since the magnitude transfer function at high frequencies decays at a slope of -40 dB/dec. In addition, the shape of the magnitude and corresponding phase delay plots suggests that there exists higher order dynamics at high frequencies. Accordingly, we fit a transfer function to the experimental frequency response data, based on the algorithms proposed in [19] and [20].

Based on the analysis of bode plot in the previous paragraph, the order of denominator in the transfer function exceeds that of numerator by 2. As a result, a transfer function with eighth-order numerator and tenth-order denominator is fitted into frequency response data up to 5 kHz, since beyond 5-kHz inadequate sampling frequency and noise gives spurious measurements. The derived transfer function fits well with frequency response data as shown in Fig. 5 (the model was derived using the function *invfreqs* in MATLAB). All the poles are stable.

C. Model Reduction

The identified model $H(s)$ is of tenth order, which adds complexity in terms of implementing model-based control designs (such as H_∞ control design). For example, if the plant is of tenth order, the corresponding H_∞ controller is of a higher order. We use *balanced truncation*, which uses *hankel singular values* σ_i of transfer function $H(s)$. σ_i characterizes the importance for each state x_i in a balanced realization, in terms of contribution to input–output behavior [21]. By implementing a balanced realization, the importance of each state is easily estimated and then it is possible to remove certain unimportant states from the original model without significant change system behavior. The Hankel singular values for the identified system $H(s)$ are shown in Fig. 6. The last two singular values, which belong to ninth and tenth state, respectively, are negligible compared to other singular values and thus are removed. The system response of the simplified model is shown in Fig. 5 along with results from the experiment and identified model. The reduced model matches well with both experimentally observed response and the identified model.

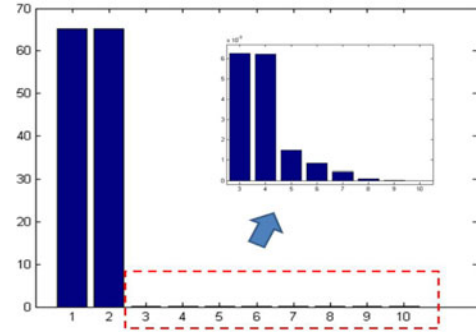


Fig. 6. Hankel singular values of $H(s)$.

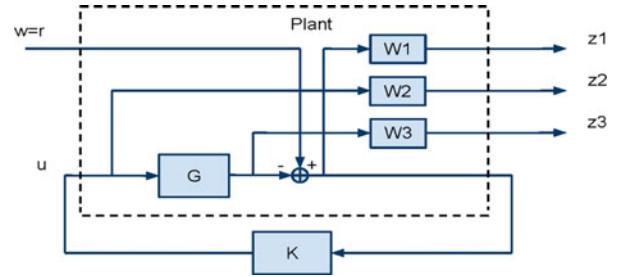


Fig. 7. $S/KS/T$ mixed-sensitivity minimization in standard form (tracking).

error $e = r - y$ even in the presence of external disturbances d and sensor noise n . Since in the closed-loop system $e = (1 + GK)^{-1}r + GK(1 + GK)^{-1}n - G(1 + GK)^{-1}d$, the design goals translate to having high bandwidth ω_S of the sensitivity transfer function $S = (1 + GK)^{-1}$ and low corner frequency ω_T for the complementary sensitivity T . In addition, we aim at making peak magnitude value of the S transfer function since it gives a measure of robustness to modeling uncertainty, and KS to be small in all frequencies since it is a measure of control effort (note $u = KSr$). The model inferred earlier for the device was employed to design the feedback laws. The feedback laws are constrained to provide control signals that were within actuator saturation limits. Besides these implementation constraints, the presence of right half plane (RHP) zeros impose fundamental constraints. From classical root locus analysis [21], we know that as the feedback gain increases, the closed-loop poles migrate to open loop zeroes, which implies high gain instability of the system. Hence, high-gain feedback laws are not applicable. They also impose a fundamental limit on the achievable bandwidth of the closed-loop system (see [21] for details). We chose H_∞ control design as it provides a systematic method to achieve the multiple objectives under these constraints.

The main advantage of using H_∞ control design is that it includes the objectives of tracking and resolution in the problem formulation. More precisely, the control law is obtained as a solution to an optimization problem which incorporates the performance objectives such as high bandwidth and high resolution in its cost function. This eliminates the tedious task of tuning the gains in the more common proportional-integral-derivative (PID) architecture.

The general setup of H_∞ control design is shown in Fig. 7. Here, the performance specifications are cast as optimization

IV. H_∞ CONTROL DESIGN

The primary objective of the control design is to achieve precise tracking of arbitrary input signals with high bandwidth. This objective is well described in terms of the closed-loop schematic in Fig. 3. The goal is to achieve small tracking

problem whose objective is to minimize a norm on a weighted matrix transfer function from exogenous inputs (r , d , and n) to regulated variables ($r-y$, u , y) (see [22]–[24] for more details about H_∞ control theory). More specifically, the weight functions W_1 , W_2 , and W_3 are chosen in a way such that

$$\left\| \begin{bmatrix} W_1 S \\ W_2 KS \\ W_3 T \end{bmatrix} \right\|_\infty$$

is minimized, where a norm is defined as the maximum of the absolute values of all the functions in the vector over the whole domain which, in this case, all frequencies. This means that each of $\|W_1 S\|_\infty$, $\|W_2 KS\|_\infty$, and $\|W_3 T\|_\infty$ is bounded by this minimum, named as γ , over all possible K . In other words, $|S|$, $|KS|$, and $|T|$ are bounded by $|\gamma/W_1|$, $|\gamma/W_2|$, and $|\gamma/W_3|$ over all frequencies. Therefore, the controller design problem comes down to choose proper weight functions W_1 , W_2 , and W_3 and achieve the minimal γ by computer optimization over all possible controllers. Indeed, S is the transfer function from reference to error and also that from disturbance to system output. Also, S indicates the robustness of a closed-loop system against model uncertainty. T is not only the transfer function from reference to system output but also that from noise to system output. KS is the transfer function from disturbance to control effort and also from reference to control effort. Thus, by bounding S , T , KS by γ/W_1 , γ/W_3 , and γ/W_2 , respectively, desired closed-loop system performances (e.g., closed-loop bandwidth, noise reduction, robustness, and stability) are guaranteed.

An important part of H_∞ control design is determining weight functions W_1 and W_3 . W_2 is left to empty in this case since we can always reduce the range of input to cut down control effort if necessary and the disturbance is a very small signal. From the previous discussion, $1/W_1$ and $1/W_3$ are the desired upper bound for S and T , respectively, if we assume $\gamma = 1$. Thus, we choose W_1 to be a low-pass filter with the bandwidth ω_S and W_3 to be a high-pass filter with the bandwidth ω_T ; that is, W_1 and W_3 are in forms given by

$$W_1 = \frac{s/M + \omega_S}{s + \omega_S A} \quad \text{and} \quad W_3 = \frac{s + \omega_T/M}{As + \omega_T}. \quad (6)$$

W_1 is equal to $1/A$ at very low frequencies and drops down to $1/M$ at very high frequency. The crossover frequency for W_1 is around ω_S . Similarly, W_3 is equal to $1/M$ at very low frequencies and rises up to $1/A$ at very high frequency. The crossover frequency for W_3 is around ω_T . Since ω_T , as an indicator of noise sensitivity, goes up as ω_S increases, we choose ω_S to be around 60 Hz and correspondingly ω_T to be around 70 Hz for good noise attenuation. A small M that is slightly over 1 means good stability while a small A leads to good robustness at low frequencies and also noise reduction at high frequencies. Accordingly, we choose $A = 1/1000$, $M = 2$ in this paper.

By implementing the H_∞ control module in MATLAB, a tenth-order controller is obtained with the constant $\gamma = 1.086$. Thus, S and T are bounded by γ/W_1 , γ/W_3 , respectively, which indicates that the design objectives are almost accomplished. Due to processor limitations, it is difficult to directly

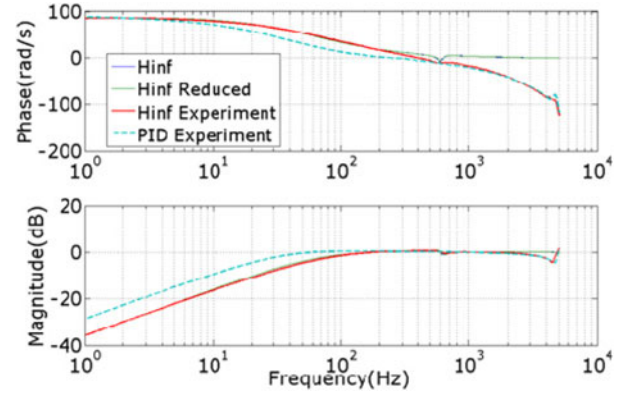


Fig. 8. Sensitivity function S : experimental versus simulation.

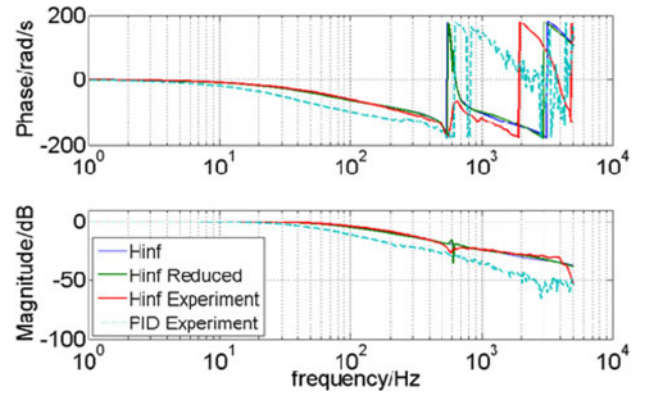


Fig. 9. Transfer function T : experimental versus simulation.

implement this continuous time controller in the dSpace control board. Again, model reduction is implemented to reduce the order and the simplified controller is discretized to improve implementation efficiency. The Hankel singular values are thus obtained. The last two states are removed and thus the order is cut down to eighth, due to implementation limitation imposed by the dSpace control board used in this paper. Given a continuous time filter, a bilinear transformation is implemented to transform it into a discrete-time representation. Further reading about bilinear transformation can be referred to [25].

V. EXPERIMENTAL RESULTS

Experimentally obtained sensitivity function S and transfer function T through DSA are shown in Figs. 8 and 9, respectively. The experimental results match well with simulation up to 500 Hz beyond which the time delay of dSpace hardware is dominant. These results indicate bandwidths given by $\omega_S = 68$ Hz and $\omega_T = 74$ Hz, around 260% better compared with PID control on the same system ($\omega_S = 26$ Hz and $\omega_T = 32$ Hz) [16]. Step response and tracking performance experimental results are presented in Figs. 10 and 11, respectively. The positioning resolution by the closed-loop system is shown in Fig. 12. The results are based on 10 000 samples taken from each output. The resolution is down to $0.0531 \mu\text{m}$. This is a better result in terms of noise reduction compared to that given by an open-loop system as also shown in Fig. 12. Moreover, robustness is

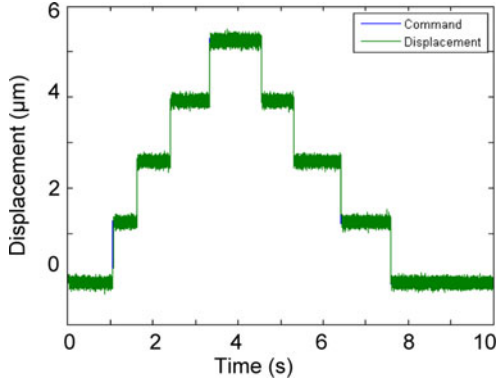
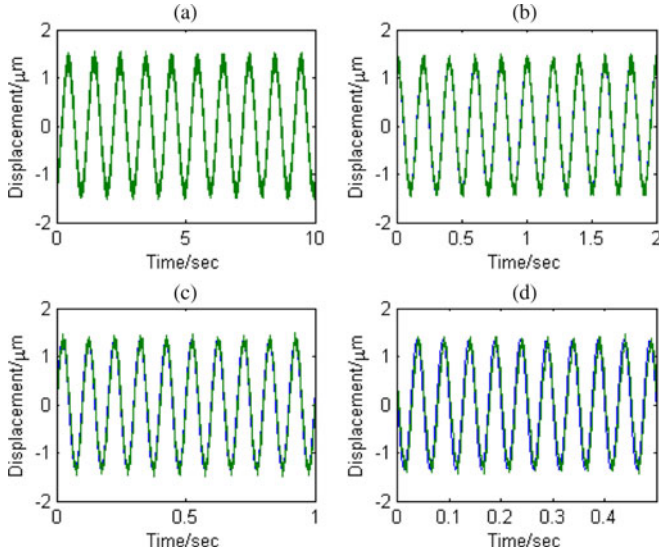
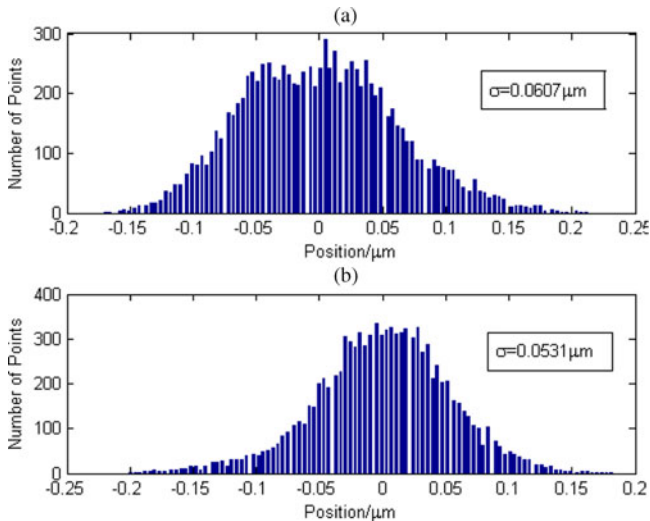
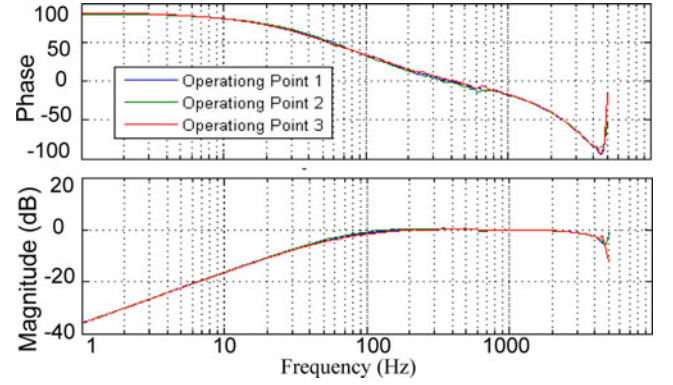
Fig. 10. Step response of the closed-loop system with H_∞ controller.Fig. 11. Tracking performances of the closed-loop system based on H_∞ controller: command (sinusoidal inputs of (a) 1 Hz (b) 5 Hz, (c) 10 Hz, and 20 Hz) in blue and displacement in green. The attenuation in the steady-state amplitudes and phase lags matches well with the bode plot in Fig. 11.

Fig. 12. Histogram of measured comb drive positions around a steady-state position: a) open loop, b) closed loop.

Fig. 13. Achieved sensitivity function S at different operating points.

verified through running the feedback system at different operating points (see Fig. 13).

By these experimental results shown here, the design objectives are realized by H_∞ controller implemented in embed control board. A high-closed-loop bandwidth ω_S is achieved along with correspondingly small ω_T which indicates a good noise reduction as shown in Fig. 12. From the time-domain responses, an excellent tracking performance by the obtained closed-loop system is verified along with impressive closed-loop stability as there is hardly any overshoot in step responses. The H_∞ control thus renders a feedback system with desired bandwidth, low noise sensitivity, enhanced stability, robustness against disturbance, and model uncertainty, which are crucial for controlling MEMS scale probing devices.

VI. CONCLUSION AND FUTURE DIRECTIONS

A MEMS probing device, which is driven by electrostatic comb drive, and its control design, are presented in this paper. This MEMS device is modeled as a linear time-invariant system and has a mechanical dynamics that is similar to a typical underdamped second-order system. The driving force F is proportional to V^2 where V is the supply voltage for the comb drive. A universal capacitance readout IC is implemented with output voltage that changes linearly with input capacitance. The displacement of comb drive around the operating point is thus estimated by the feedback signal. The model for XY stage combined with the capacitance sensor is identified and further simplified by a model reduction method.

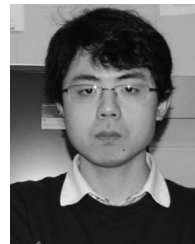
The control design process for high-bandwidth MEMS probing device control is described in this paper. The main idea behind it is to balance closed-loop bandwidth and noise attenuation, stability, and robustness. The target bandwidth ω_S is set to be around 60 Hz, which leaves room for improving other closed-loop performances such as noise reduction. Model reduction is further implemented to reduce the order of the continuous time controller from tenth to eighth due to implementation limitations. The bilinear transformation is also applied to obtain the discrete-time version of the H_∞ controller which is further implemented in dSpace control board. While it is difficult to directly compare the results from our device with results of others devices and methods, because of their different plant, the H_∞

controller renders a significantly improved closed-loop bandwidth (around 260% better compared to what we were able to obtain with PID control on the same system), good noise reduction, and excellent stability despite large model uncertainty universally existing in MEMS scale devices.

In this paper, the displacement control of comb drive along a single axis is achieved, which paves the way for feedback control of XY stage positioning. The future work thus includes designing a H_∞ controller for a MIMO system, which has position references for each of X - and Y -axis as inputs and measured positions as outputs.

REFERENCES

- [1] W. C. Tang, T. C. Nguyen, M. W. Judy, and R. T. Howe, "Laterally driven polysilicon resonant microstructures," *Sens. Actuators*, vol. 20, pp. 25–32, 1989.
- [2] B. Borovic, C. Hong, X. M. Zhang, A. Q. Liu, and F. L. Lewis, "Open vs. Closed-loop control of the mems electrostatic comb drive," in *Proc. 13th Mediterr. Conf. Control Autom.*, Limassol, Cyprus, Jun. 2005, pp. 982–988.
- [3] J. Dong and P. Ferreira, "Simultaneous actuation and displacement sensing for electrostatic drives," *J. Micromech. Microeng.*, vol. 18, art. no. 035011 (10 pp.), Jan. 2008.
- [4] P. F. Indermuhle, V. P. Jaeklin, J. Brugger, C. Linder, N. Rooij, and M. Binggeli, "AFM imaging with an xy-micropositioner with integrated tip," *Sens. Actuators*, vol. 46/47, pp. 562–565, 1995.
- [5] S. Devasia, E. Eleftheriou, and S. O. R. Moheimani, "A survey of control issues in nanopositioning," *IEEE Trans. Control Syst. Technol.*, vol. 15, no. 5, pp. 802–823, Sep. 2007.
- [6] S. Salapaka and M. Salapaka, "Scanning probe microscopy," *IEEE Control Syst. Mag.*, vol. 28, no. 2, pp. 65–83, Apr. 2008.
- [7] C. Lee and S. Salapaka, "Fast robust nanopositioning—A linear matrix inequalities based optimal control approach," *IEEE/ASME Trans. Mechatronics*, vol. 14, no. 4, pp. 414–422, Aug. 2009.
- [8] C. Lee and S. Salapaka, "Robust broadband nanopositioning: Fundamental tradeoffs, analysis and design in two degree of freedom control framework," *Nanotechnology*, vol. 20, no. 3, art. no. 035501 (16 pp.), 2009.
- [9] A. Sebastian, J. P. Cleveland, and M. V. Salapaka, "Robust control approach to atomic force microscopy," in *Proc. IEEE Conf. Decision Control*, 2003, pp. 3443–3444.
- [10] S. Salapaka, A. Sebastian, J. P. Cleveland, and M. V. Salapaka, "High bandwidth nano-positioner: A robust control approach," *Rev. Sci. Instrum.*, vol. 73, pp. 3232–3241, 2002.
- [11] A. Sebastian and S. Salapaka, "Design methodologies for robust nanopositioning," *IEEE Trans. Control Syst. Technol.*, vol. 13, no. 6, pp. 868–876, Nov. 2005.
- [12] J. Bryzek, A. Flannery, and D. Skurnik, "Integrating microelectromechanical systems with integrated circuits," *IEEE Instrum. Meas. Mag.*, vol. 7, no. 2, pp. 51–59, Jun. 2004.
- [13] J. I. Seeger and B. E. Boser, "Charge control of parallelplate, electrostatic actuators and the tip-in instability," *J. Microelectromech. Syst.*, vol. 12, no. 5, pp. 656–671, Oct. 2003.
- [14] J. Dong, D. Mukhopadhyay, and P. M. Ferreira, "Design, fabrication and testing of silicon-on-insulator (SOI) mems parallel kinematics xy stage," *J. Micromech.*, vol. 17, no. 6, pp. 1154–1161, 2007.
- [15] J. Dong and P. M. Ferreira, "Electrostatically actuated cantilever with SOI-MEMS parallel kinematic xy stage," *IEEE/ASME J. Microelectromech. Syst.*, vol. 18, no. 3, pp. 641–651, Jun. 2009.
- [16] B. Koo, X. Zhang, J. Dong, S. Salapaka, and P. M. Ferreira, "A 2 degree-of-freedom SOI-MEMS translation stage with closed loop positioning," *IEEE/ASME J. Microelectromech. Syst.*, vol. 20, no. 1, pp. 13–22, Feb. 2012.
- [17] S. Polit and J. Dong, "Development of a high-bandwidth xy nanopositioning stage for high-rate micro/nano manufacturing," *IEEE/ASME Trans. Mechatronics*, vol. 16, no. 4, pp. 724–733, Aug. 2011.
- [18] MS3110 Datasheet, Irvine Sensors Corporation, Costa Mesa, CA.
- [19] E. Levis, "Complex-curve fitting," *IRE Trans. Autom. Control*, vol. AC-4, pp. 37–44, 1959.
- [20] J. Dennis, Jr. and R. Schnabel, *Numerical Methods for Unconstrained Optimization and Nonlinear Equations*. Englewood Cliffs, NJ: Prentice-Hall, 1983.
- [21] S. Skogestad and I. Postlethwaite, *Multivariable Feedback Control: Analysis and Design*. New York: Wiley, 1996.
- [22] K. Glover and J. Doyle, "State-space formulae for all stabilizing controllers that satisfy an H₂ norm bound and relations to risk sensitivity," *Syst. Control Lett.*, vol. 11, pp. 167–172, 1988.
- [23] J. Doyle, K. Glover, P. Khargonekar, and B. Francis, "Statespace solutions to standard h₂ and H₂ control problems," *IEEE Trans. Autom. Control*, vol. 34, no. 8, pp. 831–847, Aug. 1989.
- [24] J. Dong, S. M. Salapaka, and P. M. Ferreira, "Robust control of a parallel kinematic nano-positioner," *ASME J. Dyn. Syst. Meas. Contr.*, vol. 130, no. 4, pp. 041007-1–041007-15, 2008.
- [25] Y. Matsuno, *Bilinear Transformation Method*. Orlando, FL: Academic, 1984.



Xuemeng Zhang received the B.S degree in instrumentation and controls from Tsinghua University, Beijing, China, and the M.S. degrees in mechanical engineering and mathematics from the University of Illinois at Urbana-Champaign, Urbana-Champaign, in 2008 and 2011, respectively.

He is currently involved in warehouse automation and robotics at Elettric 80, Inc., Skokie, IL.



Bonjin Koo received the Bachelor's degree in mechanical engineering from Purdue University, West Lafayette, IN, in 2008. He is currently working toward the Master's and Doctoral degrees in the Department of Mechanical Science and Engineering, University of Illinois at Urbana-Champaign, Urbana-Champaign.

His research interests include micro/nano manufacturing and system control in micro/nano scale.



Srinivasa M. Salapaka was born in Andhra Pradesh, India, in 1973. He received the B.Tech. degree from the Indian Institute of Technology Madras, Chennai, India, in 1995, and the M.S. and Ph.D. degrees from the University of California at Santa Barbara, in 1997 and 2002, respectively, all in mechanical engineering.

From 2002 to 2004, he was a Postdoctoral Associate in the Laboratory for Information and Decision Systems, Massachusetts Institute of Technology, Cambridge. Since 2004, he has been a faculty member of the Department of Mechanical Science and Engineering, University of Illinois at Urbana-Champaign, Urbana-Champaign.

His current research interests include controls for nanotechnology, combinatorial resource allocation, and numerical analysis.

Dr. Salapaka received a National Science Foundation CAREER Award in 2005.



Jingyan Dong received the B.S. degree in automatic control from the University of Science and Technology of China, Hefei, China, in 1998, the M.S. degree from the Chinese Academy of Sciences, Beijing, China, in 2001, and the Ph.D. degree in mechanical engineering from the University of Illinois at Urbana-Champaign, Urbana-Champaign, in 2006.

Since 2008, he has been a faculty member in the Department of Industrial and Systems Engineering, North Carolina State University, Raleigh, where he is currently an Assistant Professor. From 2006 to 2008, he was a Postdoctoral Researcher with the Center for Chemical-Electrical-Mechanical Manufacturing Systems at the University of Illinois at Urbana-Champaign. His research interests include micro/nano manufacturing, multi-scale mechatronics systems, and biomedical manufacturing.



Placid M. Ferreira received the B.E. degree in mechanical engineering from the University of Bombay, Mumbai, India, in 1980, the M.Tech. degree in mechanical engineering from the Indian Institute of Technology Bombay, Mumbai, in 1982, and the Ph.D. degree in industrial engineering from Purdue University, West Lafayette, IN, in 1987.

He is the Department Head and Grayce Wicall Gauthier Professor of Mechanical Science and Engineering at the University of Illinois at Urbana-Champaign, Urbana-Champaign. From 2003 to 2009, he was the Director of the Center for Chemical-Electrical-Mechanical Manufacturing Systems, the National Science Foundation (NSF) sponsored nanoscale science and engineering center. He was a member of the mechanical engineering faculty at the University of Illinois at Urbana-Champaign, in 1987, where he was the Associate Head for graduate programs and research from 1999 to 2002. His research interests include nanomanufacturing, precision engineering, and machine tools.

Dr. Ferreira received the NSF's Presidential Young Investigator Award in 1990, Society of Manufacturing Engineers' Outstanding Young Investigator Award in 1991, and the University of Illinois' University Scholar Award in 1994. He became a Fellow of the Society of Manufacturing Engineers in 2011.